PROJECTIVE ELECTRICAL IMPEDANCE RECONSTRUCTION WITH TWO MEASUREMENTS[*]

MUNKH-ERDENE TS[†], EUNJUNG LEE[‡], JIN KEUN SEO[†], BASTIAN HARRACH[§], AND SUNGWHAN KIM[¶]

Abstract. This paper presents a projective reconstruction method of electrical impedance distribution using two boundary measurements of current-voltage data. The proposed method has a major advantage over existing electrical impedance tomography systems: relatively high resolution impedance image in a near-surface region underneath the voltage-sensing probe that is placed on a skin surface. We attach two pairs of electrodes on the border of the probe in such a way that each pair of electrodes generates electrical current flowing underneath the voltage-sensing probe and two currents flow across each other. A careful analysis of the measured data with respect to local perturbation of admittivity leads to the projective reconstruction method and its rationale. Numerical simulations show that the proposed method successfully reconstructs high resolution image of local perturbation of admittivity, due to object position changes or admittivity value changes or the both, in a near-surface region underneath the probe.

Key words. electrical impedance tomography, potential theory, reconstruction algorithm

AMS subject classifications. 49N45, 35J25, 65M32

DOI. 10.1137/120879671

1. Introduction. In electrical impedance tomography (EIT), it is most common to attach electrodes at equal spacing around an imaging object such as the human body to provide cross-sectional images of an internal impedance distribution. Electrical currents are sequentially injected by changing combinations of pairs of electrodes, and the induced boundary voltages are measured on some or all of the electrodes [1, 6, 8, 17, 24, 29]. EIT uses all the current-voltage data taken at electrodes to reconstruct an image of inner impedance distribution inside the imaging object. EIT seems to be a unique technique capable of monitoring impedance changes of the patients for a long time at a low cost; it has been applied to dynamic pulmonary monitoring, stomach emptying, and more.

It is well known that the current-voltage data in EIT is insensitive to a local perturbation of inner admittivity, whereas it is heavily dependent on the boundary geometry and electrode position. Experiences show that it is very difficult to deal with the forward modeling errors caused by the boundary geometry errors and un-

certainties in electrode positions. Hence, it would be desirable to pay attention to difference EIT imaging methods where voltage data sets measured at two different times or frequencies are utilized to produce time-difference or frequency-difference, respectively, images of the admittivity distribution [15, 17, 24, 26, 30, 31, 39].

Since the late 1970s, there have been numerous reconstruction methods for EIT imaging: impedance camera [38], backprojection EIT algorithm [4, 6, 28], one-step Newton [9], layer stripping [35], D-bar [20], factorization method [7, 16, 19], and their variations. However, there still exists difficulty in achieving high quality images with a practical EIT system. The major reason is that the measurement sensitivity decreases rapidly with increasing distance from electrodes. Hence, the measurement sensitivity is very low to local perturbation of the impedance distant from the voltage-sensing electrodes. For details, see the review papers [5, 8, 23].

Admitting the fundamental limitations of EIT methods in providing a high resolution image for the interior region away from the boundary, it would be desirable to pay attention to a high resolution impedance image in a near-surface region. In theory, the layer stripping method by Somersalo et al. [35] provides a good reconstruction near the boundary; if we apply a current with a rapid spatial variation on the surface, the induced current does not penetrate very deeply into the body, and therefore the boundary voltage difference is affected mainly on the impedance change near the boundary. Hence, if the measurement error is sufficiently small, we may achieve a high resolution image in a near-surface region. However, it is difficult to get accurate voltage measurements on current injection electrodes due to the effect of contact impedance at the skin-electrode interface. The most accurate EIT model is the complete electrode model that includes the electrode-skin contact impedance [10, 34]. But, we have difficulties in obtaining accurate knowledge of electrode-skin impedances that vary from electrode to electrode [13, 21]. This inaccurate knowledge of the contact impedance produces serious image reconstruction artifacts in a near-surface region.

Lately, we proposed a new EIT system that has a unique electrode configuration and associated data collection method [22]. There has been much research using electrode configuration with a planar or circular array of sensing electrodes: EIT using a probe with a compact array of electrodes placed over the breast [11], EIT using rectangular electrode arrays [25], EIT using two plates of planar arrays of electrodes with the breast between them [12, 18], T-scan using a probe with an array of current-sensing electrodes to measure exit currents induced by an applied voltage [2, 3, 32, 33], and EIT using a hemisphere geometry [36]. Unlike all the above approaches, in this new system, two pairs of driving electrodes are attached on the four sides of the surface of the body, and an array of many voltage-sensing electrodes is attached on the surface as shown in Figure 2.1. The advantage of the separation of current injection and voltage sensing electrodes is that no current flows through the contact impedance of a voltage sensing electrode, and therefore the contact impedance contributions on measured voltage values are negligible. When we inject current using a pair of driving electrodes, the induced internal current will flow underneath the voltage sensing electrodes, and we can measure voltages between equipotential lines in the normal direction to the voltage sensing electrode array. This novel data collection method is different from those of other frontal plane techniques such as the impedance camera [38] and T-scan imaging methods [3, 33] because we do not get any data on the plane that is perpendicular to the current flow. This paper [22] focuses on analyzing the structure of electrode configuration, setting up the corresponding algorithm, and showing successful numerical simulation results.

In this paper, we give a thorough mathematical analysis of a new EIT system which has not been explored in [22]. We conduct the sensitivity analysis on the measured boundary voltage data to the time changes of interior admmitivity. Through this analysis, we explain the reasons why we obtain high resolution reconstructed images for near surface area and why the reconstructed images of the area further away from the surface appear blurry. We also introduce a deblurring process to improve these blurry reconstructed images. In the proposed new method, the measuring surface is composed of numerous voltage sensing electrodes which are placed between two pairs of current injection electrodes as shown in Figure 2.1. Similar management for voltage sensing electrodes is a pigeon hole imaging based on simple back-projection algorithm [27]. Once we describe an admittivity image reconstruction algorithm which is well-posed for a projected image and provide a mathematical analysis, we will show various numerical simulation results to verify our theory.

2. Methods. In this section, a method to reconstruct a projected image of admittivity distribution in the human abdomen using time difference Dirichlet voltage data is proposed and the mathematical analysis is presented. Let the human body be a three-dimensional domain Ω with its boundary $\partial\Omega$. The complex admittivity γ depends on time t and position $\mathbf{r} = (x, y, z)$ in Ω denoted by

$$\gamma(t, \mathbf{r}) = \sigma(t, \mathbf{r}) + i\omega\epsilon(t, \mathbf{r})$$

with $\sigma(t, \mathbf{r})$ conductivity, $\epsilon(t, \mathbf{r})$ the permittivity, and ω angular frequency. We attach two pairs of driving electrodes, $\mathcal{E}_\pm^1$ and $\mathcal{E}_\pm^2$, and an array of sensing electrodes on the surface $\partial\Omega$ as shown in Figure 2.1. When a sinusoidal current of I mA at angular frequency ω is applied through a pair of electrodes $\mathcal{E}_\pm^j$ for $j = 1, 2$, the resulting complex potential $u^j(t, \mathbf{r})$ satisfies the following boundary value problem:

(2.1)
$$\begin{cases} \nabla \cdot (\gamma(t, \mathbf{r})\nabla u^j(t, \mathbf{r})) = 0 & \text{in } \Omega, \\ \gamma(t, \mathbf{r})\dfrac{\partial u^j(t, \mathbf{r})}{\partial\mathbf{n}} = g(\mathbf{r}) & \text{on } \partial\Omega, \end{cases}$$

where $\mathbf{n}$ is the unit outward normal vector to the boundary $\partial\Omega$ and g is the corresponding Neumann boundary condition on $\partial\Omega$. To be precise, for $j = 1, 2$

(2.2) $$\int_{\mathcal{E}_\pm^j} g(\mathbf{r}) = \pm I, \quad \int_{\mathcal{E}_\pm^k} g(\mathbf{r}) = 0 \quad (k \neq j), \quad \text{and} \quad g(\mathbf{r}) = 0 \quad \text{on } \partial\Omega \setminus (\mathcal{E}_\pm^1 \cup \mathcal{E}_\pm^2).$$

Let Γ represent a portion of $\partial\Omega$ where an array of sensing electrodes is placed (see Figure 2.1). Through the probe Γ we measure the time varying boundary voltage

(2.3) $$f^j(t, \cdot) := u^j(t, \cdot)|_\Gamma \qquad \text{for } j = 1, 2.$$
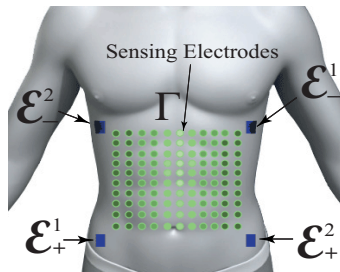

FIG. 2.1. *Electrode configuration.*

The goal is to reconstruct the time changes of complex admittivity distribution, $(\partial\gamma/\partial t)/\gamma$, underneath the probe Γ at the moment t_0 using the time change of voltage $\partial f^j/\partial t$ on Γ.

2.1. Sensitivity analysis of the projected image reconstruction method. First we describe sensitivity analysis on surface Laplacian of measured voltage to the time changes of interior admittivity. For notational convenience, fix time $t = t_0$ and denote

$$u_t^j(\mathbf{r}) := \frac{\partial}{\partial t}u^j(t_0,\mathbf{r}), \quad f_t^j(\mathbf{r}) := \frac{\partial}{\partial t}f^j(t_0,\mathbf{r}), \quad \gamma_t(\mathbf{r}) := \frac{\partial}{\partial t}\gamma(t_0,\mathbf{r}), \quad \gamma(\mathbf{r}) := \gamma(t_0,\mathbf{r}),$$

(2.4)
$$\mathbf{J}^j(\mathbf{r}) := -\gamma(t_0,\mathbf{r})\nabla u^j(t_0,\mathbf{r}) \quad \text{for } j = 1,2$$

with $\nabla = (\partial_x, \partial_y, \partial_z)^T$. We assume $\gamma_t(\mathbf{r}) = 0$ except the interior of a local region D which is compactly imbedded in Ω. Let $\Phi(\mathbf{r},\mathbf{r}')$ be the fundamental solution to the equation $\nabla \cdot (\gamma(\mathbf{r}')\nabla v(\mathbf{r}')) = 0$, where $\gamma(\mathbf{r}')$ is defined in the entire space by a standard extension. Define $\nabla_s^2 := (\mathbf{n} \times \nabla) \cdot (\mathbf{n} \times \nabla)$ as the surface Laplacian along the measuring surface Γ. In practice, the surface Laplacian is computed based on interpolated potentials [37]. Note that the surface gradient ∇_s is expressed as

$$\nabla_s = -\mathbf{n} \times (\mathbf{n} \times \nabla) = \nabla - \mathbf{n}(\mathbf{n} \cdot \nabla).$$

We denote the double layer potential of a function $\phi \in L^2(\partial\Omega)$ by

$$\mathcal{D}\phi(\mathbf{r}) = \int_{\partial\Omega} \gamma(\mathbf{r}')\frac{\partial\Phi(\mathbf{r},\mathbf{r}')}{\partial\mathbf{n}_{\mathbf{r}'}}\phi(\mathbf{r}')dS_{\mathbf{r}'} \quad \text{for } \mathbf{r} \notin \partial\Omega.$$

From the well-known trace formula for the double layer potential (see [14] for the details about trace operator), we have

$$\lim_{s\to 0^+} \mathcal{D}\phi(\mathbf{r} \pm s\mathbf{n}(\mathbf{r})) = \left(\mp\frac{1}{2}I + \mathcal{K}\right)\phi(\mathbf{r}) \quad \text{for } \mathbf{r} \in \partial\Omega,$$

where $\mathcal{K}\phi(\mathbf{r}) = \int_{\partial\Omega} \gamma(\mathbf{r}')(\partial\Phi(\mathbf{r},\mathbf{r}')/\partial\mathbf{n}_{\mathbf{r}'})\phi(\mathbf{r}')dS_{\mathbf{r}'}$ for $\mathbf{r} \in \partial\Omega$. Under the above definitions and assumptions, the following lemma holds.

LEMMA 2.1. *For $j = 1$ and 2, the surface Laplacian of the measurable quantity $(\frac{1}{2}I - \mathcal{K})f_t^j$ on Γ satisfies*

(2.5) $$\nabla_s^2\left(\left(\frac{1}{2}I - \mathcal{K}\right)f_t^j(\mathbf{r})\right) = \int_\Omega \nabla_s^2\Phi(\mathbf{r},\mathbf{r}')\mathbf{J}^j(\mathbf{r}') \cdot \nabla\left(\frac{\gamma_t(\mathbf{r}')}{\gamma(\mathbf{r}')}\right)d\mathbf{r}' \quad \text{for } \mathbf{r} \in \Gamma.$$

Proof. For $j = 1$ and 2, applying time derivative to the governing equation in (2.1) yields

(2.6) $$\nabla \cdot \left(\frac{\partial}{\partial t}\gamma(t,\mathbf{r})\nabla u^j(t,\mathbf{r})\right) = -\nabla \cdot \left(\gamma(t,\mathbf{r})\nabla\frac{\partial}{\partial t}u^j(t,\mathbf{r})\right) \quad \text{in } \Omega.$$

Then $\nabla \cdot (\gamma(\mathbf{r}')\nabla\Phi(\mathbf{r},\mathbf{r}')) = \delta(\mathbf{r} - \mathbf{r}')$ implies

(2.7) $$u_t^j(\mathbf{r}) = \int_{\partial\Omega} \gamma(\mathbf{r}')\frac{\partial\Phi(\mathbf{r},\mathbf{r}')}{\partial\mathbf{n}_{\mathbf{r}'}}u_t^j(\cdot,\mathbf{r}')dS_{\mathbf{r}'} - \int_\Omega \gamma(\mathbf{r}')\nabla\Phi(\mathbf{r},\mathbf{r}') \cdot \nabla u_t^j(\cdot,\mathbf{r}')d\mathbf{r}'.$$

Since the Neumann data g in (2.1) is independent of time t and the equality (2.6) holds, the second term in the right side of (2.7) can be expressed as

$$\int_\Omega \gamma(\mathbf{r}')\nabla\Phi(\mathbf{r},\mathbf{r}')\cdot\nabla u_t^j(\mathbf{r}')\,d\mathbf{r}'$$

$$= \int_{\partial\Omega}\Phi(\mathbf{r},\mathbf{r}')\frac{\partial}{\partial t}\left(\gamma(\mathbf{r}')\frac{\partial u^j(t_0,\mathbf{r}')}{\partial\mathbf{n}_{\mathbf{r}'}}\right)dS_{\mathbf{r}'} - \int_\Omega \Phi(\mathbf{r},\mathbf{r}')\nabla\cdot\left(\gamma(\mathbf{r}')\nabla u_t^j(\mathbf{r}')\right)d\mathbf{r}'$$

$$= \int_{\partial\Omega}\Phi(\mathbf{r},\mathbf{r}')\,\frac{\partial}{\partial t}g(\mathbf{r}')\,dS_{\mathbf{r}'} + \int_\Omega \Phi(\mathbf{r},\mathbf{r}')\nabla\cdot\left(\gamma_t(\mathbf{r}')\nabla u^j(t_0,\mathbf{r}')\right)d\mathbf{r}'$$

$$= \int_\Omega \Phi(\mathbf{r},\mathbf{r}')\nabla\cdot\left(\gamma_t(\mathbf{r}')\nabla u^j(t_0,\mathbf{r}')\right)d\mathbf{r}'$$

$$= \int_\Omega \Phi(\mathbf{r},\mathbf{r}')\nabla\cdot\left(\frac{\gamma_t(\mathbf{r}')}{\gamma(\mathbf{r}')}\,\gamma(\mathbf{r}')\nabla u^j(t_0,\mathbf{r}')\right)d\mathbf{r}'$$

$$= \int_\Omega \Phi(\mathbf{r},\mathbf{r}')\left[\nabla\left(\frac{\gamma_t(\mathbf{r}')}{\gamma(\mathbf{r}')}\right)\cdot\gamma(\mathbf{r}')\nabla u^j(t_0,\mathbf{r}')\right]d\mathbf{r}'.$$

The above equality leads (2.7) to

$$(2.8)\qquad u_t^j(\mathbf{r}) = \mathcal{D}u_t^j(\mathbf{r}) + \int_\Omega \Phi(\mathbf{r},\mathbf{r}')\mathbf{J}^j(\mathbf{r}')\cdot\nabla\left(\frac{\gamma_t(\mathbf{r}')}{\gamma(\mathbf{r}')}\right)d\mathbf{r}' \quad \text{for } \mathbf{r}\in\Omega.$$

Along the measuring surface, the identity (2.8) can be expressed as

$$(2.9)\qquad \left(\frac{1}{2}I-\mathcal{K}\right)f_t^j(\mathbf{r}) = \int_\Omega \Phi(\mathbf{r},\mathbf{r}')\mathbf{J}^j(\mathbf{r}')\cdot\nabla\left(\frac{\gamma_t(\mathbf{r}')}{\gamma(\mathbf{r}')}\right)d\mathbf{r}' \quad \text{for } \mathbf{r}\in\Gamma$$

since $\mathcal{D}\phi|_{\partial\Omega} = \left(\frac{1}{2}I+\mathcal{K}\right)\phi$ on Γ. Taking the surface Laplacian to both sides of equation (2.9), we obtain the identity (2.5). □

Since we inject two linearly independent currents through $\mathcal{E}_\pm^1$ and $\mathcal{E}_\pm^2$, we have available two boundary voltage data f^j corresponding to u^j from (2.1) for $j=1,2$. Let $\mathbf{J}$ be 2×3 matrix given by

$$\mathbf{J}(\mathbf{r}) := \begin{bmatrix} \mathbf{J}^1(\mathbf{r})^T \\ \mathbf{J}^2(\mathbf{r})^T \end{bmatrix} = \begin{bmatrix} J_1^1(\mathbf{r}) & J_2^1(\mathbf{r}) & J_3^1(\mathbf{r}) \\ J_1^2(\mathbf{r}) & J_2^2(\mathbf{r}) & J_3^2(\mathbf{r}) \end{bmatrix} \quad \text{for } \mathbf{r}\in\Omega.$$

Denoting

$$\mathbf{f}_t(\mathbf{r}) := \begin{bmatrix} \left(\frac{1}{2}I-\mathcal{K}\right)f_t^1(\mathbf{r}) \\ \left(\frac{1}{2}I-\mathcal{K}\right)f_t^2(\mathbf{r}) \end{bmatrix} \quad \text{for } \mathbf{r}\in\Gamma,$$

the identity (2.5) can be rewritten as

$$(2.10)\qquad \nabla_s^2\mathbf{f}_t(\mathbf{r}) = \int_\Omega \nabla_s^2\Phi(\mathbf{r},\mathbf{r}')\left[\mathbf{J}(\mathbf{r}')\nabla\left(\frac{\gamma_t(\mathbf{r}')}{\gamma(\mathbf{r}')}\right)\right]d\mathbf{r}' \quad \text{for } \mathbf{r}\in\Gamma.$$

OBSERVATION 2.2. *Multiplying pseudoinverse* $\mathbf{J}^\dagger(\mathbf{r})$ *to the identity* (2.10) *and taking the surface divergence, we obtain*

$$(2.11)\quad \nabla_s\cdot\left(\mathbf{J}(\mathbf{r})^\dagger\nabla_s^2\mathbf{f}_t(\mathbf{r})\right) = \nabla_s\cdot\int_\Omega \nabla_s^2\Phi(\mathbf{r},\mathbf{r}')\mathbf{J}^\dagger(\mathbf{r})\mathbf{J}(\mathbf{r}')\nabla\left(\frac{\gamma_t(\mathbf{r}')}{\gamma(\mathbf{r}')}\right)d\mathbf{r}', \quad \mathbf{r}\in\Gamma.$$

The right-hand side of the above identity carries information of γ_t/γ *including its*
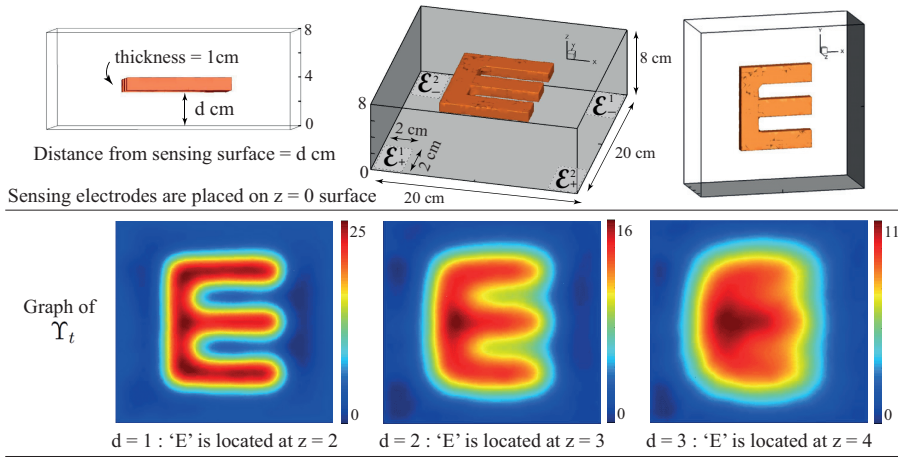
FIG. 2.2. *The solution* Υ_t *of* (2.12).

supporting region D and spatial change, and so does the left-hand side which is a measurable quantity.

Roughly speaking, if a function $\Upsilon_t : \Gamma \to \mathbb{C}$ is the solution of the two-dimensional Poisson equation

$$(2.12) \qquad \nabla_{\mathrm{s}}^2 \Upsilon_t(\mathbf{r}) = \nabla_{\mathrm{s}} \cdot \left(\mathbf{J}^\dagger(\mathbf{r}) \nabla_{\mathrm{s}}^2 \mathbf{f}_t(\mathbf{r}) \right) \quad \text{for } \mathbf{r} \in \Gamma$$

with the homogeneous boundary Neumann data, then Υ_t can be viewed as a diffusive image of γ_t / γ projected to the measuring surface Γ. Figure 2.2 shows the relation between Υ_t and γ_t / γ. Here, at time $t = 0$, the container is filled with a homogeneous material, say, $\gamma = 1$, and at $t = 0.01$, a letter "E" appears in the middle of the container with $\gamma = 3$. In order to set up the right-hand side of (2.12), we computed the right-hand side of (2.11) as follows. The current distribution $\mathbf{J}(\mathbf{r}')$ and its pseudoinverse $\mathbf{J}^\dagger(\mathbf{r})$ were obtained by numerically solving the forward problem (2.1). We took the Laplacian fundamental solution $1/(4\pi|\mathbf{r} - \mathbf{r}'|)$ as $\Phi(\mathbf{r}, \mathbf{r}')$ and calculated γ_t / γ pointwise. Then the Poisson equation (2.12) was numerically solved, and the solution Υ_t is presented in Figure 2.2.

For a better understanding of the solution Υ_t in (2.12), we simplify the model and provide sensitivity analysis on the right quantity of (2.10) in the following subsection.

2.2. Planar model. We assume that Ω is the upper half-space $\mathbb{R}_+^3$ and $\Gamma \subset \partial\Omega$, the xy-plane. We also assume the admittivity γ at time $t = t_0$ is a constant. Under these assumptions, the surface Laplacian becomes $\nabla_{\mathrm{s}}^2 = \partial_x^2 + \partial_y^2$ and Φ in (2.10) is now the fundamental solution for the Laplace operator, $\Phi(\mathbf{r}, \mathbf{r}') = 1/(4\pi|\mathbf{r} - \mathbf{r}'|)$ with $\mathbf{r} = (x, y, z) \in \Gamma$ and $\mathbf{r}' = (x', y', z') \in \Omega$. Then (2.10) transforms to

$$(2.13) \quad \nabla_{\mathrm{s}}^2 \mathbf{f}_t(\mathbf{r}) = \frac{1}{4\pi} \int_\Omega \left(\frac{(x-x')^2 + (y-y')^2 - 2(z')^2}{((x-x')^2 + (y-y')^2 + (z')^2)^{\frac{5}{2}}} \right) \mathbf{J}(\mathbf{r}') \nabla \left(\frac{\gamma_t(\mathbf{r}')}{\gamma(\mathbf{r}')} \right) \, d\mathbf{r}'$$

for $\mathbf{r} \in \Gamma$. For fixed z', let $(x-x')^2 + (y-y')^2 = \alpha^2 (z')^2$ for some α, and then we have

$$\frac{(x-x')^2 + (y-y')^2 - 2(z')^2}{((x-x')^2 + (y-y')^2 + (z')^2)^{\frac{5}{2}}} = \frac{\alpha^2 - 2}{(\alpha^2 + 1)^{\frac{5}{2}}} \frac{1}{|z'|^3} =: h(\alpha, z').$$

Figure 2.3 describes the behavior of $h(\alpha, z')$. The magnitude of function $h(\alpha, z')$ has a maximum at $\alpha = 0$ and quickly decays as α grows for fixed z'. Notice that $h(\alpha, z')$
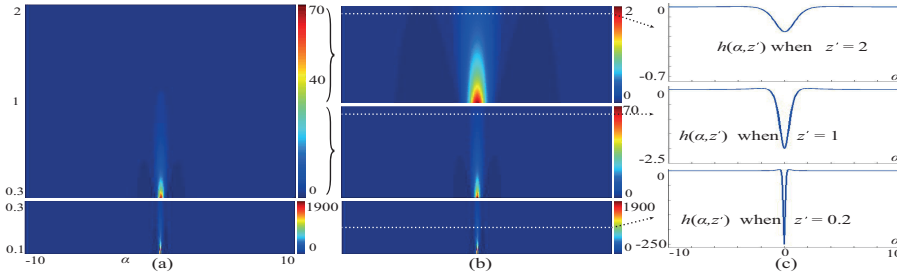
FIG. 2.3. (a), (b) $|h(\alpha, z')|$ in different scales; (c) $h(\alpha, z')$ when $|z'| = 0.2, 1$, and 2.
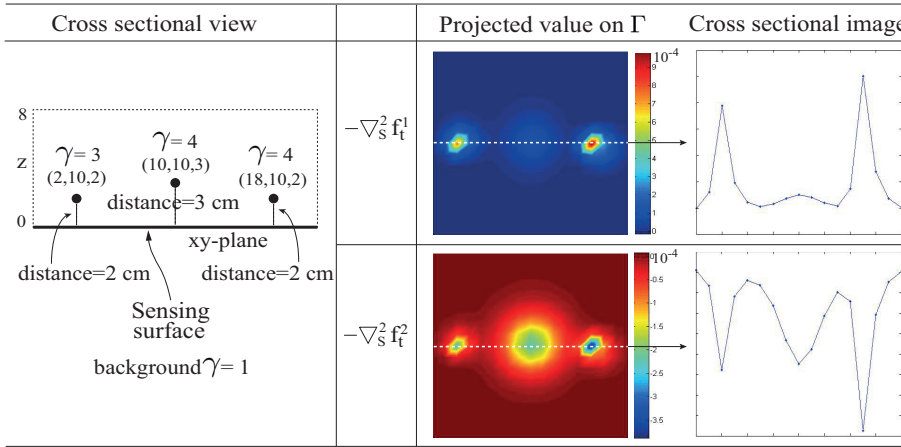

FIG. 2.4. The right-hand side of (2.13).

resembles the Dirac delta function $\delta(r)$ with $r = \sqrt{(x - x')^2 + (y - y')^2}$. Also, once $|z'|$ gets bigger, the overall function values vanish no matter what α is.

In Figure 2.4, we draw the right-hand side of (2.13) according to each $j = 1, 2$. In the computation, the domain Ω is set as a hexagon of $(0, 20) \times (0, 20) \times (0, 8)$ cm^3 and two pairs of driving electrodes are placed at four corners of bottom surface. When $t = t_1$, the container is filled with homogeneous material with $\gamma = 1$, and at $t = t_2$, there appear three objects. Three objects are spheres with the same diameter, 1 cm, that are located along $y = 10$. The center of first object is located at $(2,10,2)$ with $\gamma = 3$ and distance 2 cm from sensing surface Γ. The second object is located at $(10,10,3)$ with $\gamma = 4$ and distance 3 cm from Γ. The third object is located at $(18,10,2)$ with $\gamma = 4$ and distance 2 cm from Γ. As in Figure 2.4, it follows that the graph of $\nabla_{\mathrm{s}}^2 f_t^j(\mathbf{r})$ has relatively tall and narrow humps just above objects and the height of each hump depends on the time change of logarithm of admittivity in D as well as the distance from the sensing surface.

Based on the analysis of $\nabla_{\mathrm{s}}^2 \Phi(\mathbf{r}, \mathbf{r}')$ given above, if $\mathbf{r} \in \Gamma$ is away from the driving electrodes and the perturbed area D is located close to the sensing surface, then we have the following approximation: $\mathbf{J}(\mathbf{r}')$ can be approximated by $\mathbf{J}(\mathbf{r})$. In order to verify this approximation, we rewrite the right-hand side of (2.13) as

$$(2.14) \quad \underbrace{\int_\Omega \nabla_{\mathrm{s}}^2 \Phi(\mathbf{r}, \mathbf{r}') \left(\mathbf{J}(\mathbf{r}') - \mathbf{J}(\mathbf{r}) \right) \nabla \left(\frac{\gamma_t(\mathbf{r}')}{\gamma(\mathbf{r}')} \right) d\mathbf{r}'}_{(a)} + \underbrace{\int_\Omega \nabla_{\mathrm{s}}^2 \Phi(\mathbf{r}, \mathbf{r}') \mathbf{J}(\mathbf{r}) \nabla \left(\frac{\gamma_t(\mathbf{r}')}{\gamma(\mathbf{r}')} \right) d\mathbf{r}'}_{(b)}$$

TABLE 2.1
The values of $|(a)|$ and $|(b)|$ in (2.14).

Object	d(cm)	$\alpha = 0.02$, $\mathbf{r} = (10, 10, 0)$		center of object : (10,10, z)
		$|(a)|$	$|(b)|$	
Thickness = 0.5 cm	0.5	1.211×10^{-5}	2.025×10^{-4}	
	1	7.050×10^{-6}	2.611×10^{-4}	
	1.5	3.425×10^{-6}	3.350×10^{-4}	
Thickness = 1 cm	0.5	1.431×10^{-5}	4.718×10^{-4}	
	1	8.700×10^{-6}	5.721×10^{-4}	
	1.5	1.584×10^{-5}	7.220×10^{-4}	

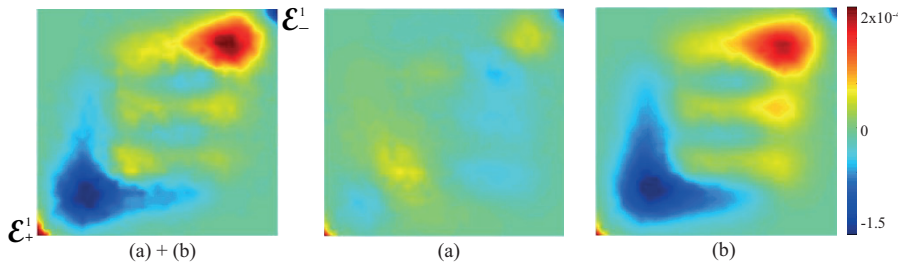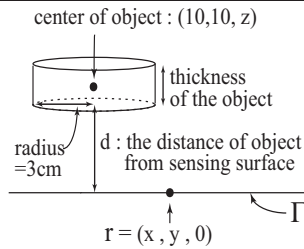| Object	d(cm)	$\alpha = 0.1$, $\mathbf{r} = (10, 10, 0)$		$\alpha = 0.1$, $\mathbf{r} = (7, 13, 0)$	
		$|(a)|$	$|(b)|$	$|(a)|$	$|(b)|$
Thickness = 0.5 cm	0.5	1.608×10^{-4}	6.584×10^{-4}	2.490×10^{-4}	7.466×10^{-4}
	1	7.092×10^{-5}	9.217×10^{-4}	1.187×10^{-4}	9.695×10^{-4}
	1.5	3.588×10^{-5}	1.287×10^{-3}	6.403×10^{-5}	1.259×10^{-3}
Thickness = 1 cm	0.5	1.524×10^{-4}	1.311×10^{-3}	5.608×10^{-4}	1.719×10^{-3}
	1	2.840×10^{-5}	1.747×10^{-3}	3.740×10^{-4}	2.093×10^{-3}
	1.5	1.525×10^{-4}	2.482×10^{-3}	3.360×10^{-4}	2.665×10^{-3}

FIG. 2.5. *Comparison of the first component in* (a)+(b), (a), *and* (b) *in* (2.14).

and compare the values of (a) and (b) in Table 2.1. In the Table 2.1, the center of a cylindrical shape of thin object (which is D in this test) is placed at $(10, 10, z)$ with various $z > 0$, and let $\mathbf{r} = (x, y, 0) \in \Gamma$. The admittivity $\gamma(0, \mathbf{r}')$ is set to be 1 for all $\mathbf{r}'$ at time $t = 0$ and

$$\gamma(1, \mathbf{r}') = \begin{cases} 1 + \alpha \times x'y'z' & \text{if } \mathbf{r}' = (x', y', z') \in D \subset \Omega, \\ 1 & \text{otherwise} \end{cases}$$

at time $t = 1$ so that $\gamma_t / \gamma \equiv 0$ in $\Omega \backslash D$. The current density $\mathbf{J}$ is obtained from solving the forward problem (2.1) for each γ with the domain $\Omega = (0, 20) \times (0, 20) \times (0, 8)$ cm^3, a cubic container. As shown in the table, the value of integration with $\mathbf{J}(\mathbf{r}') - \mathbf{J}(\mathbf{r})$ is relatively smaller than the value of integration with $\mathbf{J}(\mathbf{r})$. As additional evidence, we use the "E" shape object from Figure 2.2 ($d = 1$: "E" is located at $z = 2$) and plot the overall values of (a) and (b) in (2.14) on Γ-surface in Figure 2.5. Since the value in (2.14) is a 2×1-vector where the first component is obtained when the current is injected through $\mathcal{E}_\pm^1$ and the second is from injecting current through $\mathcal{E}_\pm^2$, we only show the graph of the first component of (2.14) here. (The second component shows similar behavior.) By comparing figures in Figure 2.5, one can easily see that the image of (b) is much closer to the image of (a) + (b) than the image of (a) is.

Since $\mathbf{J}^j(\mathbf{r}) = (J_1^j(\mathbf{r}), J_2^j(\mathbf{r}), 0)^T$, $j = 1, 2$, (2.13) is comparable with

$$(2.15) \qquad \nabla_s^2 \mathbf{f}_t(\mathbf{r}) \approx \left[\begin{array}{cc} J_1^1(\mathbf{r}) & J_2^1(\mathbf{r}) \\ J_1^2(\mathbf{r}) & J_2^2(\mathbf{r}) \end{array} \right] \int_\Omega \nabla_s^2 \Phi(\mathbf{r}, \mathbf{r}') \nabla_{s'} \frac{\gamma_t}{\gamma}(\mathbf{r}') d\mathbf{r}',$$

where $\nabla_{s'} = (\partial_{x'}, \partial_{y'})^T$. Therefore, we conclude

$$(2.16) \qquad \nabla_s^2 \mathbf{f}_t(\mathbf{r}) = \left[\begin{array}{cc} J_1^1(\mathbf{r}) & J_2^1(\mathbf{r}) \\ J_1^2(\mathbf{r}) & J_2^2(\mathbf{r}) \end{array} \right] \left(\nabla_s \frac{\gamma_t(\mathbf{r}')}{\gamma(\mathbf{r}')} \right)_{\mathrm{Pr}}, \quad \mathbf{r} \in \Gamma, \ \mathbf{r}' \in D,$$

where $(\nabla_s(\gamma_t/\gamma))_{\mathrm{Pr}}$ is a projected value of $\nabla_s(\gamma_t/\gamma)$ which is magnified and localized by the Newtonian potential in D onto Γ-surface. Since only the boundary voltage data on Γ is available, current components J_1^j and J_2^j can be approximated as

$$(J_1^j, J_2^j) \approx -\nabla_s f^j \quad \text{for } j = 1, 2.$$

Now we construct the projected image reconstruction algorithm using time difference voltage data to provide the projected image of the interior admittivity distribution which is parallel to the measuring surface.

OBSERVATION 2.3. *Let* $\mathbf{f} = [f^1 \ f^2]^T$ *with* f^j *the measured boundary voltage data as in* (2.3). *If* $\Upsilon_t(\mathbf{r})$ *is the solution of*

$$(2.17) \qquad -\nabla_s^2 \, \Upsilon_t(\mathbf{r}) \ = \ \nabla_s \cdot \left((\nabla_s \, \mathbf{f}(\mathbf{r}))^{-1} \nabla_s^2 \, \mathbf{f}_t(\mathbf{r}) \right) \quad \text{for } \mathbf{r} \in \Gamma,$$

then $\Upsilon_t(\mathbf{r})$ *provides a projected image of* γ_t/γ *in the interior of the body onto the sensing surface,* Γ.

We recall the "E" shape of object which was used in Figure 2.2. The same size of container and electrode configuration in Figure 2.2 are used and a total of 1089 (33×33) sensing electrodes are placed on top of the container for boundary voltage measurements. Instead of solving (2.12) to obtain Υ_t, we now use the proposed algorithm introduced in Observation 2.3 to obtain Υ_t. Figure 2.7 shows the reconstructed image of projected γ_t/γ. Comparing with the results in Figure 2.2, the proposed algorithm provides similar Υ_t.

2.3. Deblurring. When an object is located further away from the sensing surface, the reconstructed projected image Υ_t (obtained from (2.17)) is getting more and more blurred; see Figure 2.6. We can improve the reconstructions by the following simple deblurring strategy.

We consider the reconstructed image Υ_t as a function of the true conductivity change and define $G : \frac{\gamma_t}{\gamma} \mapsto \Upsilon_t$, where Υ_t solves (2.17). It is aimed to invert this
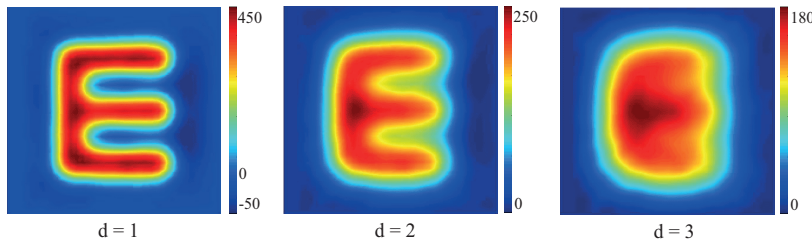

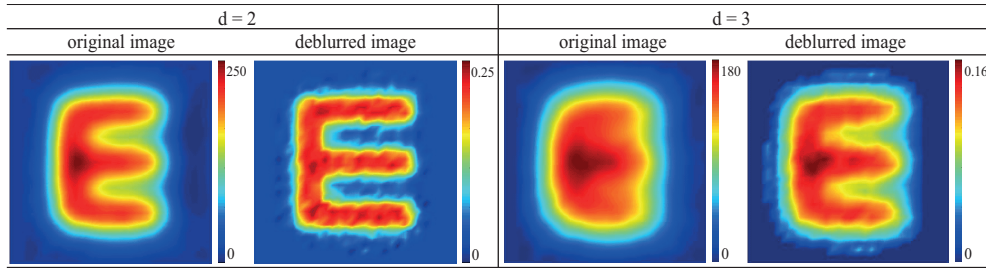FIG. 2.6. *The solution* Υ_t *of* (2.17): *distance from sensing surface* $= d$ *cm.*

| d = 2 | | d = 3 | |
| original image | deblurred image | original image | deblurred image |

FIG. 2.7. *The deblurred images of solution* Υ_t *of* (2.17).

nonlinear mapping in order to obtain a better approximation of γ_t/γ from the blurred reconstructions Υ_t. To that end we replace G by its linearized version (noting that $G(0) = 0$)

$$(2.18) \qquad \Upsilon_t = G(\gamma_t/\gamma) \approx G'(0)\frac{\gamma_t}{\gamma}.$$

It is not realistic to reconstruct the full three-dimensional distribution of γ_t/γ from the two-dimensional images Υ_t. We therefore solve (2.18) in the subspace of three-dimensional conductivity distributions that are zero up to depth d and constant along the z-direction below this depth and interpret the solution as a two-dimensional projected image of γ_t/γ. $G'(0)$ is approximated by finite differences.

We apply the suggested deblurring process to the blurred reconstructed images obtained in Figure 2.6 for d = 2 cm and d = 3 cm and show the results in Figure 2.7.

3. Numerical simulations. In this section, we use the boundary voltage data **f** obtained from sensing electrodes to reconstruct the image of internal admittivity distribution parallel to the sensing surface by solving (2.17). The finite element method is used for every numerical simulation.

3.1. Hexagonal container model. Let $\Omega = (-5.5, 5.5) \times (-5.5, 5.5) \times (0, 4)$ be a hexagonal container as shown in Figure 3.1. In the container, three static objects are placed with different admittivity (see Figure 3.2) and one changing object is placed between them. First, we change the position of object in time. Then we fix the position and change the admittivity or size of the object.

Example 3.1. One tetrahedron with side length 0.5 cm is counted as an object with $\gamma = 7$, and the center of it moves from $(-1, 1, 1.5)$ at $t = 0$ to $(3, -0.5, 1.5)$ at $t = 0.1$ as shown in Figure 3.3(a). Figure 3.3(b) shows the reconstructed image of γ_t/γ. Here, the magnitude of reconstructed γ_t/γ at time $t = 0.1$ is relatively smaller than the magnitude of γ_t/γ at time $t = 0$ since the contrast of γ is smaller $(3(= 7 - 4)$
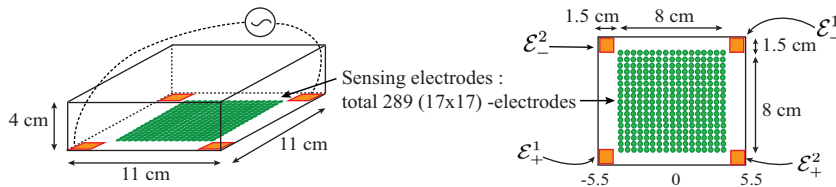

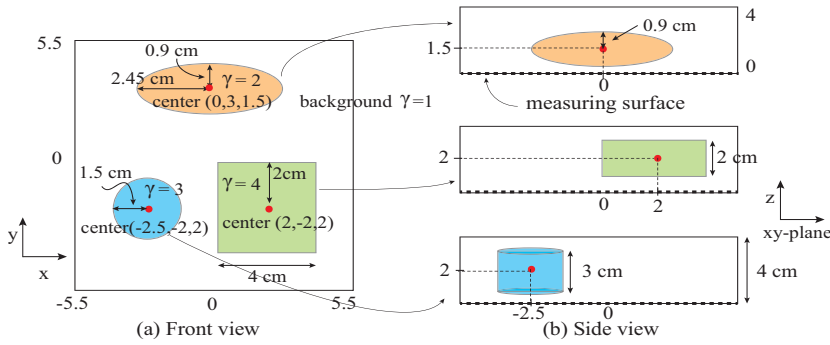FIG. 3.1. *Numerical simulation domain: driving and sensing electrodes.*

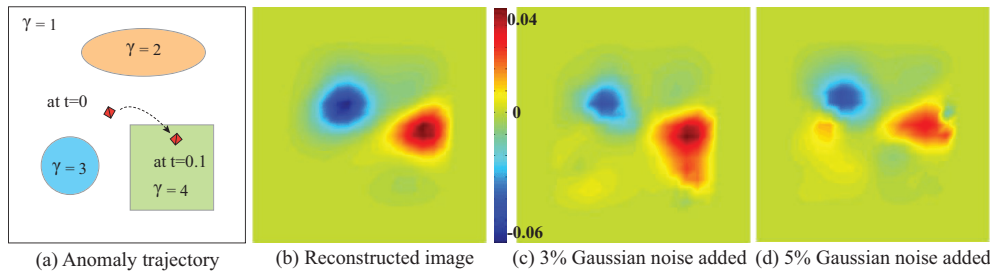Fig. 3.2. *The locations of static objects in the hexagonal container.*

(a) Anomaly trajectory   (b) Reconstructed image   (c) 3% Gaussian noise added (d) 5% Gaussian noise added

Fig. 3.3. *Reconstructed image of γ_t/γ when time changes from $t = 0$ to $t = 0.1$ with moving object (fixed admittivity and changed position): (b) without any noise (c) 3% Gaussian random noised added to the data (d) 5% Gaussian random noised added.*
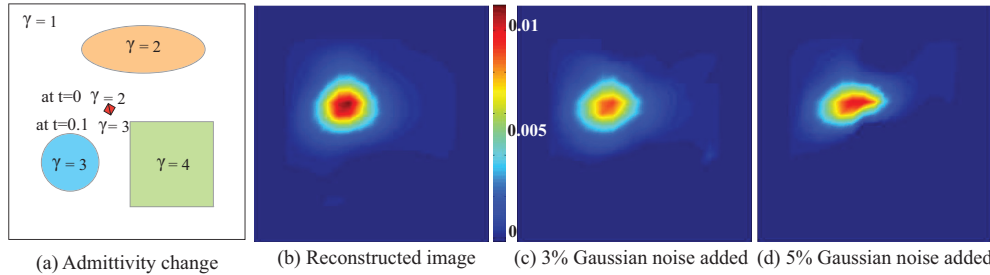

(a) Admittivity change   (b) Reconstructed image   (c) 3% Gaussian noise added (d) 5% Gaussian noise added

Fig. 3.4. *Reconstructed image of γ_t/γ when time changes from $t = 0$ to $t = 0.1$ with admittivity changing object (changed admittivity and fixed position): (b) without any noise (c) 3% Gaussian random noised added to the data (d) 5% Gaussian random noised added.*

vs. $6(= 7-1)$. Figures 3.3(c), (d) are the reconstructed images of γ_t/γ when Gaussian random noises are added to the measured voltage.

Example 3.2. In this example, we fix one tetrahedron at $(-1, 1, 1.5)$ with side length 0.5 cm as an anomaly and change the admittivity $\gamma = 2$ at $t = 0$ to 3 at $t = 0.1$ as shown in Figure 3.4. Figure 3.4 also contains the reconstructed image of γ_t/γ when Gaussian random noises are added.

Example 3.3. This example shows the reconstructed image of γ_t/γ in the presence of multiple anomalies. We set three anomalies in different positions, centered at $(2, 2.5, 2)$, $(-1.5, 1, 2)$, and $(1, -2, 2)$. All anomalies are of cylindrical shape with radius 0.8 cm and thickness 1 cm. In Figure 3.5(b), three anomalies have the same
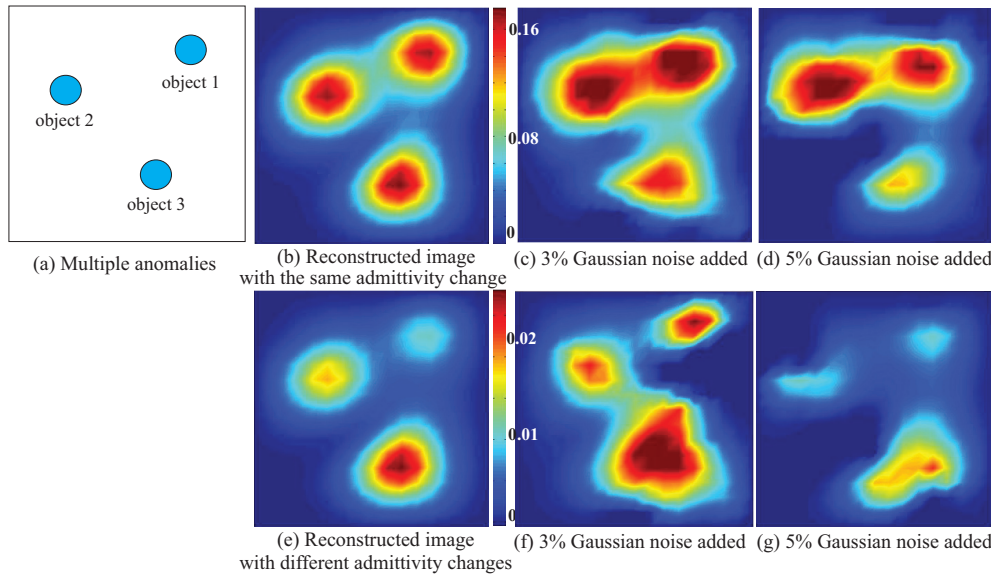
(a) Multiple anomalies   (b) Reconstructed image   (c) 3% Gaussian noise added (d) 5% Gaussian noise added
                              with the same admittivity change

(e) Reconstructed image   (f) 3% Gaussian noise added (g) 5% Gaussian noise added
with different admittivity changes

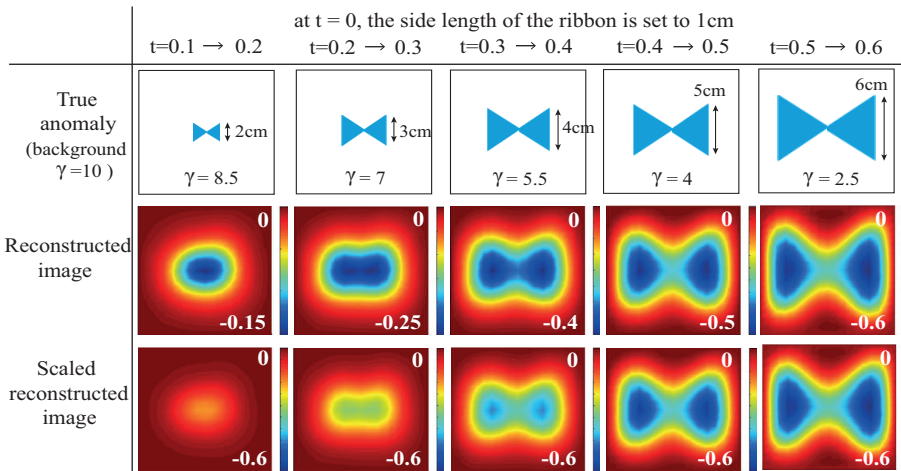FIG. 3.5. *Admittivity changing objects.*

FIG. 3.6. *A moving admittivity changing object (extension).*

admittivity change $\gamma = 3$ at $t = 0$ and $\gamma = 5$ at $t = 0.1$. Figure 3.5(c) shows the reconstructed image of γ_t/γ when each object has different admittivity change:

$$\text{object 1 centered at } (2, 2.5, 2), \quad \gamma = 3(t = 0) \implies \gamma = 4(t = 0.1),$$
$$\text{object 2 centered at } (-1.5, 1, 2), \quad \gamma = 3 \implies \gamma = 5,$$
$$\text{object 3 centered at } (1, -2, 2), \quad \gamma = 3 \implies \gamma = 6.$$

Example 3.4. A ribbon shape object is repeating consecutive extension and contraction with different admittivity. The distance of this object from the measuring surface is 1 cm and the thickness is 2 cm. We present the reconstructed image of γ_t/γ in Figure 3.6. The third row of the figure shows reconstructed images in a fixed scale.

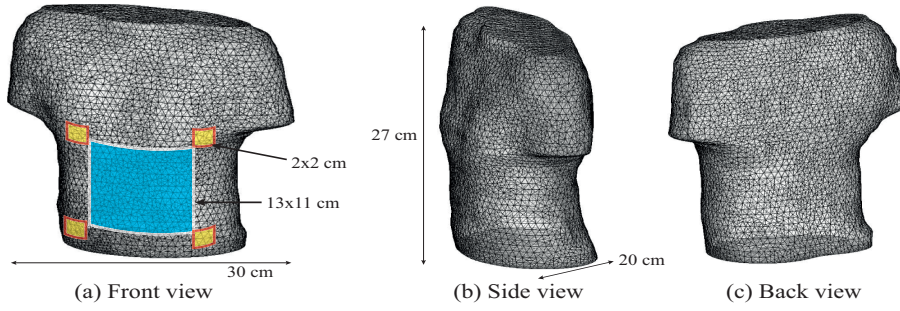(a) Front view   (b) Side view   (c) Back view

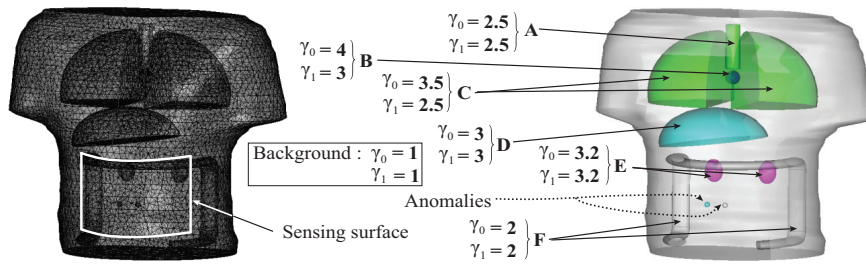FIG. 3.7. *FEM body structure: 26820 nodes, 141026 tetrahedrons.*

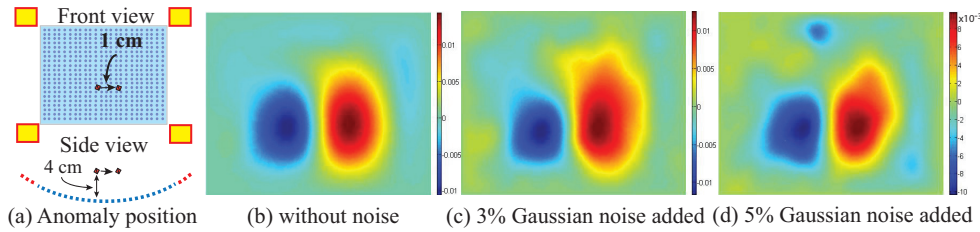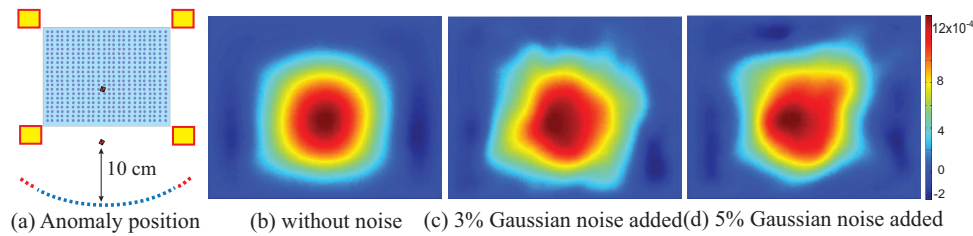FIG. 3.8. *Interior admittivity distribution: γ_j = the admittivity at time t_j for $j = 0, 1$.*

(a) Anomaly position   (b) without noise   (c) 3% Gaussian noise added (d) 5% Gaussian noise added
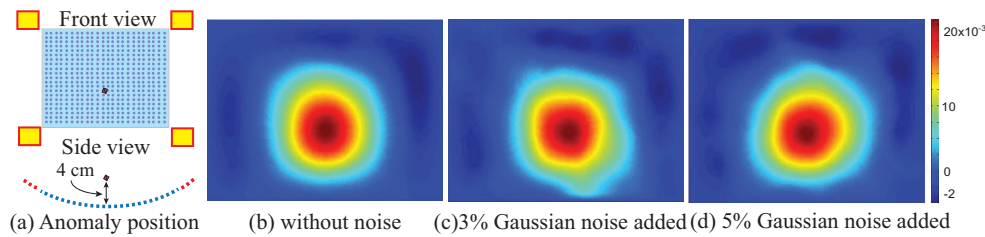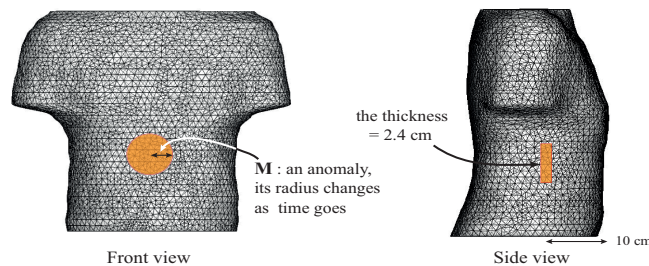
FIG. 3.9. *Torso model: reconstructed γ_t/γ-image of a moving admittivity changing object, $\gamma = 8$ at $t = 0$ and $\gamma = 7$ at $t = 0.1$.*

3.2. Torso model. In this subsection, we show the results of numerical simulations in a human body model. Here, we used COMSOL to construct a human body model to use finite element method as shown in Figure 3.7. A total of 323 (17×19) sensing electrodes are attached on the curved measuring surface. Inside of this torso model, several organs are placed with different admittivity (see Figure 3.8). Throughout this section, the background admittivity is always fixed as 1.

Example 3.5. One small object (a tetrahedron with side length less than 0.6 cm) moves 1 cm to the right as shown in Figure 3.9. The admittivity of this moving object changes from 8 (at time t_0) to 7 (at time t_1) for 0.1 second while the background admittivity is fixed as 1. The distance of the object from the measuring surface is about 4 cm. Figure 3.9 also presents the reconstructed images when Gaussian random noise is added to the collected data.

Example 3.6. Now, we fix the position of object and change the admittivity only. The size of object is the same with Example 3.5, but the position is now much further

(a) Anomaly position   (b) without noise   (c) 3% Gaussian noise added(d) 5% Gaussian noise added

FIG. 3.10. *Torso model: γ_t/γ of an admittivity changing object.*

(a) Anomaly position   (b) without noise   (c)3% Gaussian noise added (d) 5% Gaussian noise added

FIG. 3.11. *Torso model: Real part of γ_t/γ of a complex admittivity changing object.*

FIG. 3.12. *Torso model: γ_t/γ of a complex admittivity changing object.*

away from the measuring surface. The distance of the object from the measuring surface is about 10 cm and γ changes from 8 to 7 for 0.1 second as in Figure 3.10.

Example 3.7. In this example, we run test with complex admittivity. The size and position of anomaly is the same with the case $t = 0$ in Example 3.5, but γ changes from $1 + 2\pi i\omega\epsilon$ to $8 + 2\pi i\omega\epsilon$ for 0.1 second in which $\omega = 10$ Hz and $\epsilon = 6 \times 10^{-6}$. The other organ parts also have admittivity $\gamma_j + 2\pi i\omega\epsilon$, $j = 0, 1$. The results are shown in Figure 3.11.

Example 3.8. Here, we place a thin cylindrical shape object, $\mathbf{M}$, with thickness 2.4 cm as shown in Figure 3.12. The center of this object is fixed and the distance from the measuring surface is 10 cm. As time goes, the radius and admittivity of anomaly object are changing (see Table 3.1). Here the object $\mathbf{M}$ does not touch other organs. The admittivity of each organ in Figure 3.8 is given in Table 3.1, and the background admittivity is fixed as 1. Figure 3.13 shows the real values of the reconstructed image of γ_t/γ. The magnitude of imaginary part of the reconstructed value γ_t/γ is relatively small and is sensitive to the noise. Once the Gaussian noise is added, the imaginary part of reconstructed value γ_t/γ looks like a noise data.

TABLE 3.1
Radius and admittivity of the anomaly; admittivities of other parts in Figure 3.8; $\eta = 12\pi \times 10^{-5}$.

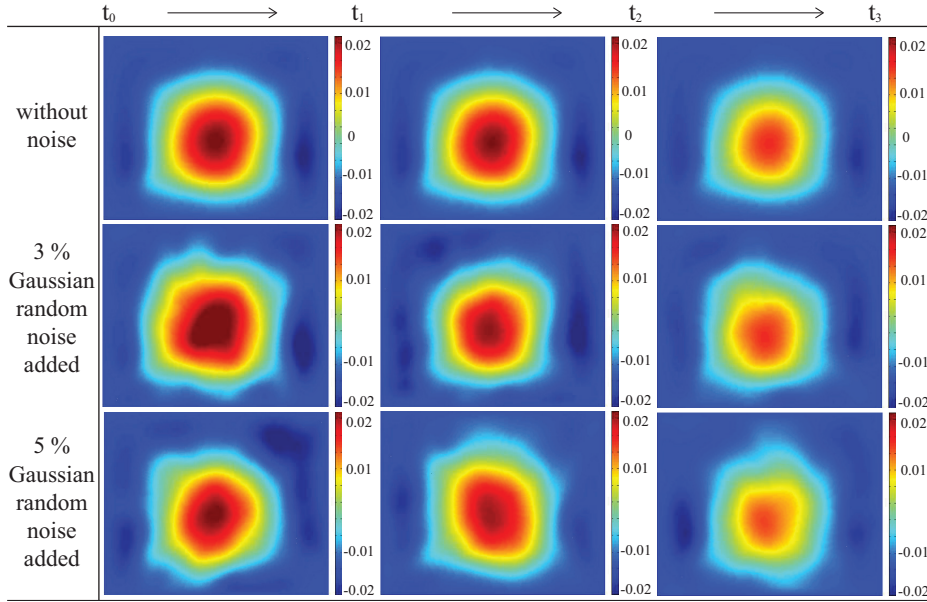| Time	Radius of **M**	γ of **M**	Admittivity (γ) changes					
			A	**B**	**C**	**D**	**E**	**F**
$t_0 = 0$	2 cm	$3.0 + i\eta$	$2.5 + i\eta$	$4.0 + i\eta$	$3.5 + i\eta$	$3 + i\eta$	$3.2 + i\eta$	$2 + i\eta$
$t_1 = 0.1$	1.6 cm	$3.2 + i\eta$	$2.5 + i\eta$	$3.8 + i\eta$	$3.3 + i\eta$	$3 + i\eta$	$3.2 + i\eta$	$2 + i\eta$
$t_2 = 0.2$	1.2 cm	$3.4 + i\eta$	$2.5 + i\eta$	$3.6 + i\eta$	$3.1 + i\eta$	$3 + i\eta$	$3.2 + i\eta$	$2 + i\eta$
$t_3 = 0.3$	0.8 cm	$3.6 + i\eta$	$2.5 + i\eta$	$3.4 + i\eta$	$2.9 + i\eta$	$3 + i\eta$	$3.2 + i\eta$	$2 + i\eta$

FIG. 3.13. *Reconstructed image of real* (γ_t/γ).

4. Discussion and conclusion. A conventional EIT system injects current into the body through a pair or more of surface electrodes and measures induced voltages on multiple surface electrodes. Utilizing boundary voltage data subject to multiple injection current patterns, it visualizes the interior admittivity distributions. While it has numerous biomedical applications as a noninvasive, portable, and low-cost medial imaging modality with high temporal resolution, the spatial resolution is low. To improve the resolution, a new direct EIT image reconstruction algorithm with a novel electrode configuration is proposed and analyzed in this paper. Through various numerical simulations, we showed reconstructed images of the internal admittivity distribution of the body using boundary voltage measurements.

As shown in Figure 2.6 and other simulation results, if an object is close to the sensing surface, then the proposed method produces high resolution images. However, if an object is located further away from the sensing surface, then we cannot avoid the blurring effect caused by the surface Laplacian of fundamental solution given in (2.11). In such cases, we suggest using a deblurring process introduced in subsection 2.3. Our future work includes minimizing these blurring effects and the usage of depth directional information. We believe that the method is promising and is worth being explored in various applications.

REFERENCES

[1] A. ADLER, J.H. ARNOLD, R. BAYFORD, A. BORSIC, B. BROWN, P. DIXON, T.J.C. FAES, I. FRERICHS, H. GAGNON, Y. GARBER, B. BRYCHTOL, G. HAHN, W.R.B. LIONHEART, A. MALIK, R.P. PATTERSON, J. STOCKS, A. TIZZARD, N. WEILER, AND G.K. WOLF, *Greit: A unified approach to* 2*D linear EIT reconstruction of lung images*, Physiological Measurement, 30 (2009), pp. S35–55.

[2] H. AMMARI, O. KWON, J.K. SEO, AND E.J. WOO, *T-Scan electrical impedance imaging system for anomaly detection*, SIAM J. Appl. Math., 65 (2004), pp. 252–266.

[3] M. ASSENHEIMER, O. LAVER-MOSKOVITZ, D. MALONEK, D. MANOR, U. NAHALIEL, R. NITZAN, AND A. SAAD, *The T-scan technology: Electrical impedance as a diagnostic tool for breast cancer detection*, Physiological Measurement, 22 (2001), pp. 1–8.

[4] D.C. BARBER AND B.H. BROWN, *Applied potential tomography*, J. Phys. E Sci. Instruments, 17 (1984), pp. 723–733.

[5] L. BORCEA, *Electrical impedance tomography*, Inverse Problems, 18 (2002), p. R99.

[6] B.H. BROWN, D.C. BARBER, AND A.D. SEAGAR, *Applied potential tomography: Possible clinical applications*, Clin. Phys. Physiol. Meas., 6 (1985), pp. 109–121.

[7] M. BRÜHL AND M. HANKE, *Numerical implementation of two noniterative methods for locating inclusions by impedance tomography*, Inverse Problems, 16 (2000), pp. 1029–1042.

[8] M. CHENEY, D. ISAACSON, AND J.C. NEWELL, *Electrical impedance tomography*, SIAM Rev., 41 (1999), pp. 85–101.

[9] M. CHENEY, D. ISAACSON, J.C. NEWELL, S. SIMSKE, AND J. GOBLE, *Noser: An algorithm for solving the inverse conductivity problem*, Int. J. Imaging Systems Technology, 2 (1990), pp. 66–75.

[10] K.S. CHENG, D. ISAACSON, J.C. NEWELL, AND D.G. GISSER, *Electrode models for electric current computed tomography*, IEEE Trans. Biomed. Eng., 36 (1989), pp. 918–924.

[11] V.A. CHEREPENIN, A.Y. KARPOV, A.V. KORJENEVSKY, V.N. KORNIENKO, Y.S. KULTIASOV, M.B. OCHAPKIN, O.V. TROCHANOVA, AND J.D. MEISTER, *Three-dimensional EIT imaging of breast tissues: System design and clinical testing*, IEEE Trans. Med. Imaging, 21 (2002), pp. 662–667.

[12] M.H. CHOI, T.J. KAO, D. ISSACSON, G.J. SAULNIER, AND J.C. NEWELL, *A reconstruction algorithm for breast cancer imaging with electrical impedance tomography in mammography geometry*, IEEE Trans. Med. Imaging, 54 (2007), pp. 700–710.

[13] E. DEMIDENKO, *An analytic solution to the homogeneous EIT problem on the* 2*D disk and its application to estimation of electrode contact impedances*, Physiological Measurement, 32 (2011), pp. 1453–1471.

[14] G.B. FOLLAND, *Introduction to Partial Differential Equations*, 2nd ed., Princeton University Press, Princeton, NJ, 1995.

[15] H. GRIFFITHS, *The importance of phase measurement in electrical impedance tomography*, Physics in Medicine and Biology, 32 (1987), pp. 1435–1444.

[16] M. HANKE AND M. BRÜHL, *Recent progress in electrical impedance tomography*, Inverse Problems, 19 (2003), pp. S65–S90.

[17] D. HOLDER, *Electrical Impedance Tomography: Methods, History and Applications*, Institute of Physics Publishing, Bristol, UK, 2005.

[18] T.J. KAO, J.C. NEWELL, G.J. SAULNIER, AND D. ISAACSON, *Distinguishability of inhomogeneities using planar electrode arrays and different patterns of applied excitation*, Physiological Measurement, 24 (2003), pp. 403–411.

[19] A. KIRSCH, *Characterization of the shape of a scattering obstacle using the spectral data of the far field operator*, Inverse Problems, 14 (1998), pp. 1489–1512.

[20] K. KNUDSEN, M. LASSAS, J.L. MUELLER, AND S. SILTANEN, *Regularized D-bar method for the inverse conductivity problem*, Inverse Problems Imaging, 3 (2009), pp. 599–624.

[21] V. KOLEHMAINEN, M. LASSAS, AND P. OLA, *Electrical impedance tomography problem with inaccurately known boundary and contact impedances*, IEEE Trans. Medical Imaging, 27 (2008), pp. 1404–1414.

[22] E. LEE, TS. MUNKH-ERDENE, J.K. SEO, AND E.J. WOO, *Breast EIT using a new projected image reconstruction method with multi-frequency measurements*, Physiological Measurement, 33 (2012), p. 751.

[23] W. LIONHEART, N. POLYDORIDES, AND A. BORSIC, *The reconstruction problem*, in Electrical Impedance Tomography: Methods, History and Applications, D. S. Holder, ed., IOP Series in Medical Physics and Biomedical Engineering, Institure of Physics Publishing, 2005, pp. 3–64.

[24] P. Metherall, D.C. Barber, R.H. Smallwood, and B.H. Brown, *Three-dimensional electrical impedance tomography*, Nature, 380 (1996), pp. 509–512.

[25] J.L. Mueller, D. Isaacson, and J.C. Newell, *A reconstruction algorithm for electrical impedance tomography data collected on rectangular electrode arrays*, IEEE Trans. Biomed. Eng., 46 (1999), pp. 1379–1386.

[26] T.I. Oh, H. Koo, K.H. Lee, S.M. Kim, J. Lee, S.W. Kim, J.K. Seo, and E.J. Woo, *Validation of a multi-frequency electrical impedance tomography (MFEIT) system KHU Mark*1: *Impedance spectroscopy and time-difference imaging*, Physiological Measurement, 29 (2008), pp. 295–307.

[27] K.S. Rabbani, M. Sarker, M.H.R. Akond, and T. Akter, *Focused impedance measurement (FIM): A new technique with improved zone localization*, Ann. New York Acad. Sci., 873 (1999), pp. 408–429.

[28] F. Santosa and M. Vogelius, *A backprojection algorithm for electrical impedance imaging*, SIAM J. Appl. Math., 50 (1990), p. 216–243.

[29] G.J. Saunier, R.S. Blue, J.C. Newell, D. Isaacson, and P.M Edic, *Electrical impedance tomography*, IEEE ASSP Magazine, 18 (2001), pp. 31–43.

[30] J.M. Scaife, R.C. Tozer, and I.L. Freeston, *Conductivity and permittivity images from an induced current electrical impedance tomography system*, Science Measurement and Technology IEE Proceedings, 141 (1994), pp. 356–362.

[31] J. Schlappa, E. Annese, and H. Griffiths, *Systematic errors in multi-frequency EIT*, Physiological Measurement, 21 (2000), pp. 111–118.

[32] B. Scholz and R. Anderson, *On electrical impedance scanning: Principles and simulations*, Electromedica, 68 (2000), pp. 35–44.

[33] J.K. Seo, O. Kwon, H. Ammari, and E.J. Woo, *Mathematical framework and anomaly estimation algorithm for breast cancer detection: Electrical impedance technique using TS*2000 *configuration*, IEEE Trans. Biomed. Eng., 51 (2004), pp. 1898–906.

[34] E. Somersalo, M. Cheney, and D. Isaacson, *Existence and uniqueness for electrode models for electric current computed tomography*, SIAM J. Appl. Math., 52 (1992), pp. 1023–1040.

[35] E. Somersalo, M. Cheney, D. Isaacson, and E. Isaacson, *Layer stripping*, Society., 7 (1991), pp. 736–754.

[36] N.K. Soni, A. Hartov, C. Kogel, S.P. Poplack, and K.D. Paulsen, *Multi-frequency electrical impedance tomography of the breast: New clinical results*, Physiological Measurement, 25 (2004), pp. 301–314.

[37] K. Wang and H. Begleiter, *Local polynomal estimate of surface Laplacian*, J. Phys. Conf. Ser., 12 (1999), p. 28.

[38] J.G. Webster, *Medical Instrumentation Application and Design*, Vol. 3, Houghton Mifflin Company, Boston, 1978.

[39] R.J. Yerworth, R. Bayford, B. Brown, P. Milnes, M. Conway, and D.S. Holder, *Electrical impedance tomography spectroscopy (EITS) for human head imaging*, Physiological Measurement, 24 (2003), pp. 477–489.